Versatile fitting approach for operando spectroscopic imaging ellipsometry of HfS_2 oxidation

2D Materials

OPEN ACCESS

RECEIVED
8 February 2024

REVISED
31 May 2024

ACCEPTED FOR PUBLICATION
17 June 2024

PUBLISHED
2 July 2024

PAPER

Versatile fitting approach for operando spectroscopic imaging ellipsometry of HfS_2 oxidation

Irina Chircă[1], AbdulAziz AlMutairi[1], Barat Achinuq[2], Rongsheng Cai[2], Sarah J Haigh[2] and Stephan Hofmann[1,*]

[1] Department of Engineering, University of Cambridge, Cambridge CB3 0FA, United Kingdom
[2] Department of Materials, University of Manchester, Oxford Road, Manchester M13 9PL, United Kingdom
[*] Author to whom any correspondence should be addressed.

E-mail: sh315@cam.ac.uk

Keywords: 2D materials, spectroscopic imaging ellipsometry, transition metal dichalcogenides, complex dielectric function, HfS_2, oxidation, operando

Supplementary material for this article is available online

Abstract

Facile mapping of 2D heterostructures and resolving anisotropic formation kinetics down to the monolayer level are critical to developing scalable interfacing solutions and unlocking their application potential in emerging nano-optoelectronics. We adapt a Kramers–Kronig constrained variational fitting algorithm for spectroscopic imaging ellipsometry (SIE) to facilitate multi-scale heterostructure analysis comprising films with unknown complex dielectric functions and demonstrate how this enables non-destructive, scalable mapping and operando capability for the model system of HfS_2 oxidation. This methodology proves highly accurate for assessing the thickness of buried HfS_2 layers, oxide quality, and lateral and vertical uniformity. We capture dynamic stack evolution during thermal oxidation up to 400 °C, providing insights into the temperature and time-dependent nature of self-limiting oxide growth and reaction kinetics that involve the localised trapping and release of sulphur reaction products. Our methodology is versatile in material and device horizons, and advantageously agnostic to the underlying substrate. Combined with the various modes of SIE operation, it unlocks fast, high-throughput, large-area capability to accelerate process development at the atomic scale.

1. Introduction

High-throughput experimental workflows and rapid feedback loops are essential to unlock much-needed accelerated materials development [1–5]. At every stage of the process, from materials discovery to manufacturing pathway discovery and quality monitoring, there is demand for characterisation approaches that can resolve complex structure-property relations down to the atomic layer level as well as enable smart, high-throughput, low-cost screening [6, 7]. Spectroscopic imaging ellipsometry (SIE) [8–12] is emerging as a powerful technique in this context, displaying versatility in both material and application horizons. Its various measurement modes not only facilitate the exploration of optical properties [13–16] and in operando growth kinetics [17–20], but also enable rapid, large-scale mapping [10, 11, 21]. Notably, SIE stands out as one of the few techniques capable of non-destructive characterisation of buried layers and interfaces [22–24], combining the advantages of optical microscopy and spectroscopic ellipsometry. For emergent 2D materials, atomic monolayer thickness resolution has been demonstrated on different substrates [9, 14], and SIE used to resolve mono-, bi-, and trilayer systems [9, 10, 12, 14].

More complex sample structures, however, highlight the current challenges of ellipsometry. For novel materials with unknown complex dielectric functions (ε), modelling the optical response requires numerous global fitting parameters [8, 9, 12–14, 25]. While prior knowledge of material properties can constrain the free parameters to physically meaningful values and accelerate convergence, widespread fitting procedures such as the Levenberg-Marquardt algorithm [9, 12, 13, 26, 27] rapidly become time-intensive and computationally taxing when applied

to highly parameterised systems [28]. 2D materials add another level of complexity: a layer-dependant dielectric response and shifting bandgap, requiring separate ε extraction at various sample thicknesses from monolayer to few-layer and bulk [9, 13, 14]. Material instabilities, e.g. degradation against ambient conditions and/or the formation of interfacial layers, present further complexities to fitting and interpretation [8]. These challenges are particularly pertinent to using SIE for operando reaction studies, where the layer number, thickness and properties are dependent on process parameters and time, i.e. are dynamically changing.

Here, we adapt a Kramers–Kronig constrained variational analysis [29] as an alternative, highly efficient fitting methodology, and demonstrate heterostructure mapping and operando capability for the model system of HfS_2 oxidation. HfS_2 is a layered semiconductor of the transition metal dichalcogenide (TMD) family [30, 31] with a stable, high-κ native oxide [32–35]. Clean, scalable interfacing remains a crucial bottleneck for 2D nanoelectronics, and such complementary semiconductor/dielectric structures are of large technological potential [36, 37], as highlighted by the historic dominance of the Si/SiO_2 system [38, 39]. Recent literature highlights promising device data from 2D semiconductors with native oxides [32–34, 40–43], including HfS_2, $HfSe_2$ and $ZrSe_2$. However, oxidation has a vast associated parameter space, from precursors to activation, including plasma, thermal annealing, and laser/photo-oxidation [33–35, 44]. Moreover, models used for bulk and conventional thin film materials, such as the Deal–Grove model for Si oxidation [45], do not straightforwardly translate to layered materials with extreme structural anisotropy. Operando capability is required to refine the understanding of reaction kinetics and to improve predictive control.

Our fitting algorithm enables the accelerated and precise determination of unknown ε, facilitating a multi-scale analysis of layered HfS_2/HfO_x heterostructures. The layer-resolved SIE mapping of partially oxidised HfS_2 areas with 1 μm lateral resolution allows for an assessment of oxide quality, homogeneity, and thickness as a function of process parameters. Simultaneously, operando oxidation experiments provide insights into the temperature and time-dependent nature of self-limiting oxide growth, revealing the formation, trapping and release of volatile sulphur species during the oxidation process.

2. Methods

2.1. Sample preparation

HfS_2 flakes are micro-mechanically exfoliated (Ultron Systems adhesive tape) from commercially available bulk crystals (HQ Graphene) on n-type doped Si wafers with a 285 nm SiO_2 layer for enhanced optical contrast. The regions of interest are identified via optical microscopy (Nikon Eclipse LV200). All sample preparation pre-oxidation is done under an Ar atmosphere inside a glovebox.

2.2. SIE

Ellipsometry measurements are performed with an EP4 SIE (Park Systems Gmbh, Göttingen), with a spectral range between 360 to 1000 nm and a $\sim$5 nm output bandwidth. The reflected light is collected through an analyzer and a 20x or 50x objective to a 1392 $\times$ 1040 pixel CCD camera, allowing for a lateral resolution down to 1 μm.

Characterisation of freshly exfoliated, unoxidised HfS_2 flakes is performed using a solid-liquid cell configuration (Park Systems Gmbh, Göttingen) set up with a continuous nitrogen flow to minimise any material oxidation. To further ensure material integrity, the cell is assembled inside the glovebox. (Ψ, Δ) spectra are recorded as a signal average over an approx. 10 μm $\times$ 10 μm homogeneous region of interest (ROI) via the single-point measurement mode at 200 equidistant λ points along the 360 to 1000 nm range.

The SIE mapping function is employed for the high-resolution imaging and characterisation of partially and fully oxidised HfS_2 samples, measured in ambient conditions at room temperature. Each map pixel encodes a complete (Ψ, Δ) spectra, which is then fitted using the EP4Model software. The thickness information is extracted for each layer as complementary 3D maps.

The HfS_2 and HfO_x thickness maps shown in figures 3(c) and (d) are fitted from an SIE image captured using a 50x magnifying objective. The total area displayed contains 203 $\times$ 237 pixels, corresponding to 58.3 μm $\times$ 68 μm. Each pixel measures approximately 0.29 μm $\times$ 0.29 μm, as recorded in the raw file metadata. No binning (defined as integrating N $\times$ N pixels of the original image into one pixel of the processed image) is applied during the data acquisition or image processing steps in order to maximise resolution. The image exhibits some edge diffusion, potentially due to optical aberrations or noise interference. Therefore, we consider the resolution accurately represented as $\sim$ 1 μm.

Operando studies are performed using single-point measurements to increase time resolution. A heating stage (Linkam) is mounted on top of the EP4 sample holder, and oxidation is monitored from 23 °C to 400 °C under ambient conditions. The signal is averaged over an approx. 10 μm $\times$ 10 μm ROI. Each (Ψ, Δ) spectra, taken at 30 equidistant λ points along the 360 to 1000 nm range, is recorded over 6 min, at 6 min intervals.

All measurements are performed in the P-A-nulling mode, at an incidence angle of 50° for ambient and operando experiments. The geometry of the

solid-liquid cell set-up requires a 65° incidence angle with respect to the surface normal.

2.3. Complementary sample characterisation

The thickness of HfS_2 and HfS_2/HfO_x heterostructures is determined via atomic force microscopy (AFM; MFP-3D Asylum System and Bruker Icon). To mitigate the effect of native oxidation, pristine HfS_2 flakes are characterized using a closed nitrogen cell (Asylum) assembled inside the glovebox.

Scanning transmission electron microscopy (STEM) images and energy dispersive x-ray (EDX) spectroscopy elemental maps of the oxidised HfS_2 samples are collected using a ThermoFisher Titan STEM (G2 80-200) equipped with a Cs probe corrector (CEOS) and ChemiSTEM Super-X EDX detector, operating at 200 kV. High-angle annular dark field STEM images are acquired using a semi-convergence angle of 21 mrad and a collection angle of 54 mrad. High-resolution transmission electron microscopy (HRTEM) imaging is performed using a ThermoFisher Talos S/TEM (F200X), operating at 200 kV. Cross-sectional TEM samples are prepared using a ThermoFisher Nova Nanolab 600 focus ion beam (FIB). A protective layer of C and Pt is deposited onto the sample surface prior to the FIB sample preparation.

3. Results and discussion

3.1. Variational fitting methodology for SIE data analysis

The analysis of multi-layer heterostructures via SIE, especially in the context of complex reactions such as material oxidation, requires an appropriate understanding of each layer's dielectric response and a representation of the sample structure, in the form of an accurate optical model. Fundamentally, since there is no direct calculation for extracting physical quantities from the ellipsometric angles (Ψ, Δ), the determination of any unknown parameters becomes a non-linear regression problem: given our best initial estimation of the sample's properties, a model set of (Ψ,Δ) is generated and compared to the measured (Ψ, Δ), referred to as the ground truth. Through an iterative adjustment of the fitting parameters, we aim to minimise the difference between the model (Ψ,Δ) and the ground truth until we converge on the 'true' value of the parameters. Consequently, prior information is initially required to facilitate convergence and build a high-accuracy model that can correctly interpret the sample's (Ψ,Δ). We follow the ellipsometric data analysis methodology outlined in figure 1: construction of an optical model describing the heterostructure of interest, modelling of ε for each constituent layer, and fitting of the predicted (Ψ, Δ) to measured (Ψ, Δ) spectra.

We model the progressive oxidation of HfS_2 as a HfS_2/HfO_x heterostructure (figure 1), with variable layer thickness parameters, from pristine HfS_2 ($d_{\text{oxide}} = 0$ nm) to fully converted HfO_x ($d_{HfS_2} = 0$ nm), with the substrate defined as Si(100) with a 285 nm SiO_2 layer. The initial material sequence is thereby informed by previous HfS_2 studies demonstrating that oxidation progresses from the topmost layer with negligible interfacial oxide between the HfS_2 and substrate [33, 34, 46]. Due to the impact of process parameters on material stoichiometry, we universally label the oxide layer as HfO_x.

It is important to note that each material is modelled as an ultra-flat, uniform layer with sharply defined interfaces, which can be difficult to attain in the context of partially oxidised heterostructures. Any deviation from the ideal optical model results in signal loss, data interpretation challenges, and reduced resolution. Generally, SIE can facilitate surface roughness analysis through the incorporation of an additional top layer into the optical model [8]. This layer would be represented by a mixture of ε_{HfO_x} and ε_{air}, and measure a few nanometres in thickness. Treating the surface roughness as a separate optical layer can be useful in quantifying the surface quality or monitoring changes in morphology. However, it introduces several highly correlated parameters into the fitting process, which can converge to multiple solutions. For instance, there can be little distinction between 5 nm of oxide with a 1 nm roughness layer and 4 nm of oxide with a 2 nm roughness layer. Therefore, we have chosen to model the oxide as a single layer and thus factor any surface roughness into the HfO_x signal.

The complex dielectric function of HfS_2 is extracted from a ~20 nm exfoliated sample via a Kramers–Kronig constrained variational analysis [29] of the raw (Ψ, Δ) spectra (figure 2). To suppress ambient oxidation [47, 48] and minimise the systematic error introduced by a native oxide layer, we measure pristine HfS_2 samples under a protective nitrogen atmosphere (see Methods). The fitting procedure is implemented using the lmfit package for Python [49], and the non-linear least-squares minimisation problem is solved using the Levenberg-Marquardt algorithm. The root mean square error (RMSE) and the unbiased RMSE values evaluate the goodness of fit.

First, we extract a rough ε by fitting the spectra to an appropriate physical model with limited global parameters to minimize computation time. We use the Tauc-Lorentz oscillator model [8], a refinement of the Lorentz oscillator allowing for the parametrisation of the bandgap absorption in semiconductors, as derived by Jellison and Modine [50]. The Tauc–Lorentz oscillator (RMSE = 2.01, unbiased RMSE = 3.01) successfully captures the indirect bandgap transition at $E_G = 2.15 \pm 0.25$ eV, which agrees with the experimentally measured values of 1.96 eV and 2.13 eV reported by Greenaway *et al* [51] and Roubi *et al* [52] for bulk HfS_2. However, given the limited number of parameters, the Tauc–Lorentz model

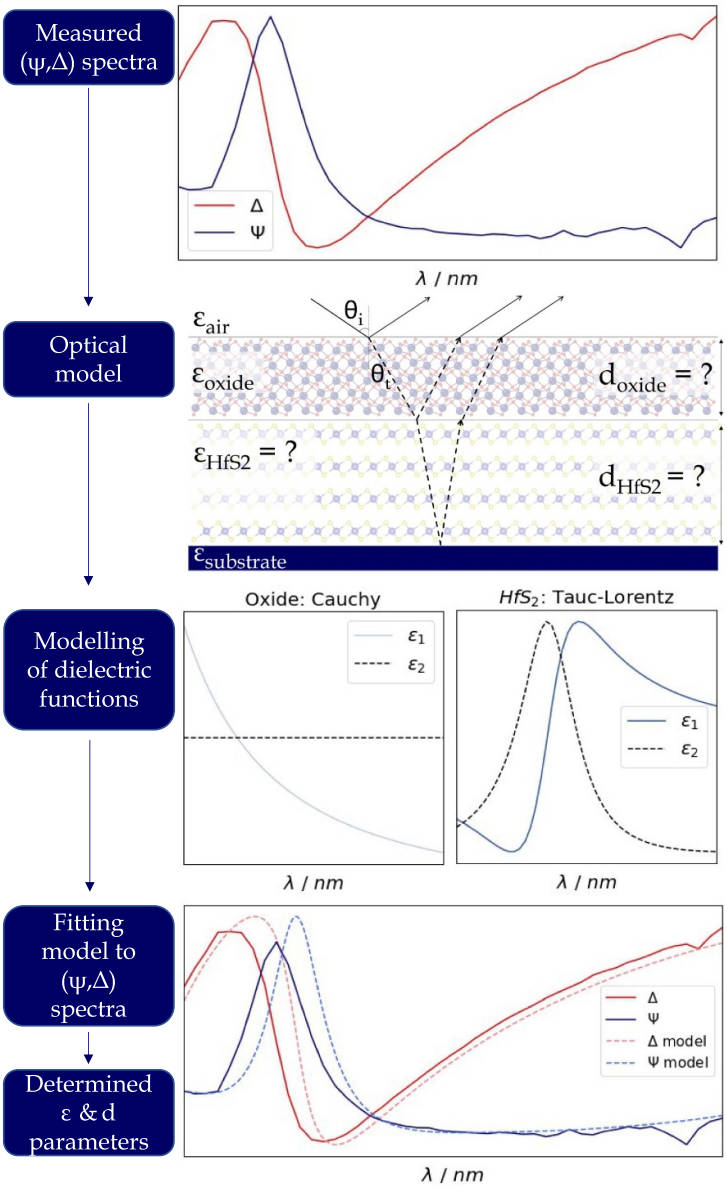

Figure 1. Ellipsometry data analysis methodology for multi-layer systems [8]: (1) Optical constants and layer thicknesses are measured from the change in polarization state upon light reflection, encoded as ellipsometric angles (Ψ, Δ) for a range of incident wavelengths. (2) Each layer is described by the material's ε and thickness parameter (d), then integrated into an optical model. (3) For materials with unknown ε, dielectric function models are assigned: a transparent insulating oxide is most often described by a Cauchy dispersion (assuming $\varepsilon_2 = 0$), while a semiconductor can be parameterised by a Tauc-Lorentz oscillator. (4) The predicted (Ψ, Δ) , as calculated from the constructed optical model, are fitted to the raw data. (5) An iterative fitting process converges on the correct thickness and dielectric function parameters, where the optical model accurately predicts the experimental result.

fails to properly represent the 360 to 500 nm optical response. Conventionally, additional Lorentz oscillators can circumvent this issue [9, 53], but the three global parameters added per oscillator exponentially increase the computational cost. Here, any 'lost' features not described by the Tauc–Lorentz oscillator are captured using the variational fitting algorithm, with a resulting RMSE of 1.18 and unbiased RMSE of 2.34. This method works as a fine correction of the rough dielectric function, treating the spectral range as a series of narrow triangular oscillators anchored equidistant between each data point [29].

From the as extracted ε_{HfS_2}, we obtain a maximum extinction coefficient (k) for HfS_2 of 4.4 at 376 nm incident wavelength. We calculate an absorption coefficient (α) of 1.46×10^6 cm^{-1} using the expression $\alpha = 4\pi\kappa/\lambda$, resulting in an approximated penetration depth (d_p) limit of 6.9 nm. The details of this calculation are expanded upon in the supplementary material (figure S1). Since the detection limit of ellipsometry measurements can be approximated to $5\times d_p$ [8, 54], we select an initial pre-oxidation thickness < 30 nm for all HfS_2 samples, thus allowing the monitoring of HfS_2/substrate interactions.

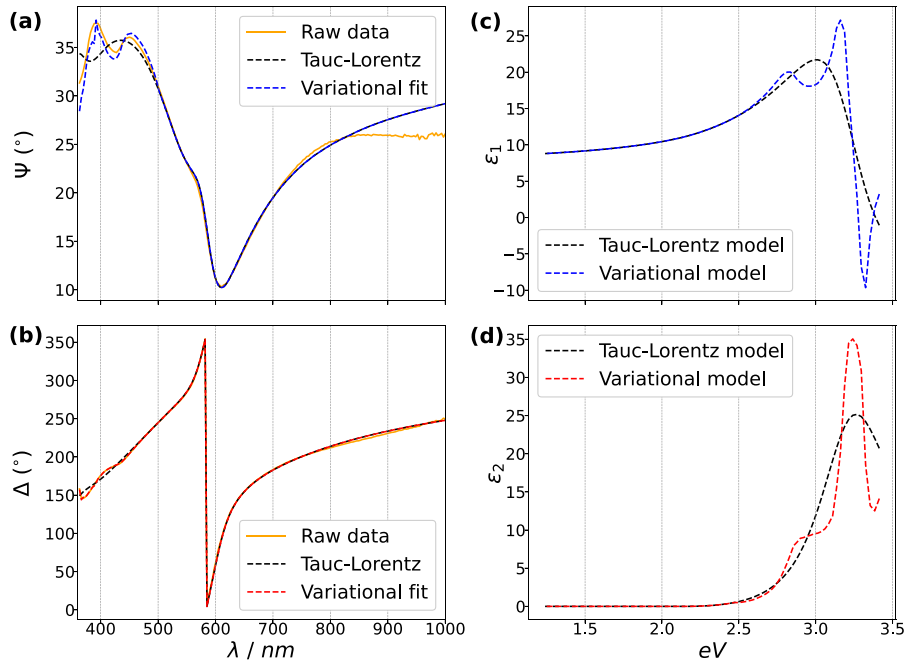

Figure 2. Ellipsometric measurement of a ∼20 nm HfS_2 flake on Si / 285 nm SiO_2 substrate under nitrogen atmosphere. (a)–(b) The (Ψ, Δ) spectra are fitted to a Tauc–Lorentz oscillator (RMSE = 2.01, unbiased RMSE = 3.01), and then further adjusted via a Kramers–Kronig constrained variational algorithm [29] (RMSE = 1.18, unbiased RMSE = 2.34). (c) The real part of the complex dielectric function (ε_1) extracted via the Tauc-Lorentz model and the variational model. (d) The imaginary part of the complex dielectric function (ε_2) extracted via the Tauc-Lorentz model and the variational model. Bandgap calculated as 2.15 ± 0.25 eV for both methodologies.

The crystal anisotropy is addressed by considering ε_{HfS_2} as a linear combination of the in-plane and out-of-plane dielectric tensors [8], and a good approximation for HfS_2 identification in the < 30 nm range. This isotropic approximation is a common approach in the ellipsometric analysis of anisotropic TMDs [13–16], since the in-plane component dominates the overall dielectric value. Future work will cover this methodology's application in capturing each component's individual parameters and creating a universally applicable model.

3.2. HfS_2/HfO_x heterostructure modelling

Once the semiconductor layer has been defined, we incorporate ε_{HfS_2} into the multi-layer $Si/SiO_2/HfS_2/HfO_x$ model, with d_{HfS_2} and d_{HfO_x} as free parameters. The complex dielectric functions for the Si, SiO_2, and HfO_x layers are implemented using the dispersion tables available in the EP4Model software library, collected from the Sopra database [55]. We assess the accuracy of this optical model against cross-sectional TEM of a partially oxidised HfS_2 sample, exposed to thermal annealing at 200 °C for 30 min in ambient conditions (figure S2 in supplementary material). TEM imaging reveals non-uniform oxidation characterised by 2.3–3.6 nm of amorphous top oxide growth and a semiconductor layer spanning 16.1–19.6 nm. Despite a considerable contrast between the field of view in TEM analysis and the μm scale signal averaging inherent in ellipsometric measurements, our model demonstrates close agreement by identifying a 3.2 nm oxide layer on top of 19.2 nm of HfS_2. This calculation is derived from signal averaging over a 1.5 μm × 5.5 μm sample area.

EDX spectroscopy elemental mapping confirms HfO_x formation and suggests the presence of S residue (9.1 atomic %) in the oxide layer (figure S3 in supplementary material). Sulphur doping is anticipated to induce a red shift in the absorbance spectra of hafnia, facilitating absorption in the visible region, as well as an increase in the real part of the complex refractive index [56]. However, the reasonable agreement between the SIE and AFM-measured oxide thickness values indicates the presence of S impurities is sufficiently low to exert minimal influence on the oxide's ε.

Notably, the high-resolution TEM (figure S2 in supplementary material) also reveals the formation of a ∼1 nm oxide layer at the SiO_2/HfS_2 interface. Previous TEM imaging of HfS_2 after plasma [33, 46] and laser-assisted oxidation [34] shows exclusively top-down oxide growth, while studies investigating HfS_2 thermal annealing and native oxidation under ambient conditions [35, 48] include no cross-sectional analysis. However, Mleczko *et al* [32] report both top and bottom oxide formation for the neighbouring Group 4 TMD ZeS_2 after 3 days of ambient exposure. We adjust the HfS_2/HfO_x model by adding an additional hafnia interlayer and refit the previous

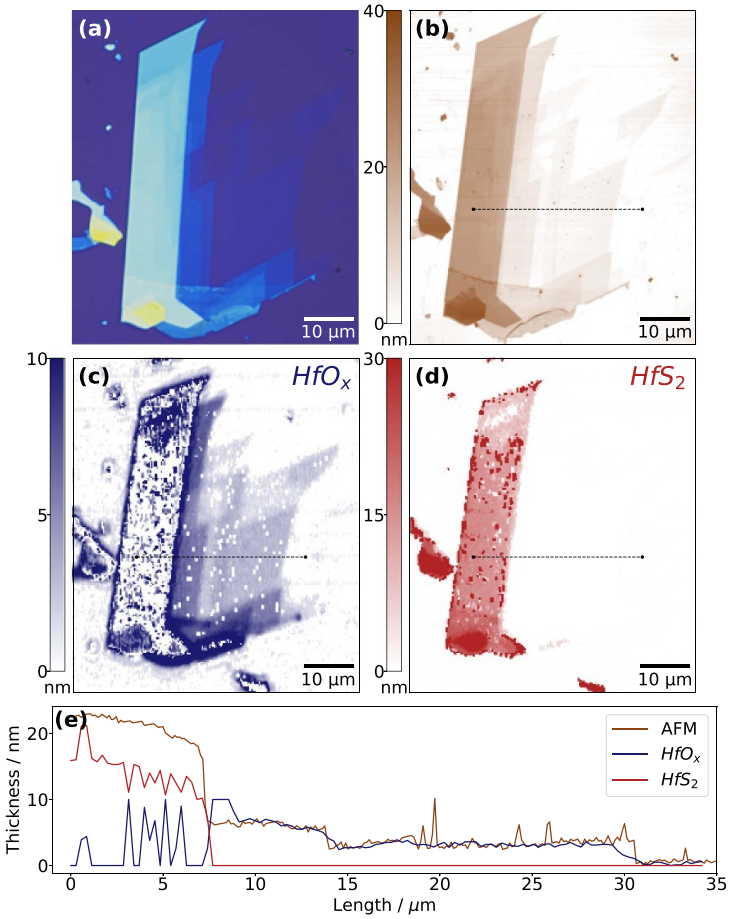

Figure 3. Imaging of partially oxidised HfS_2 on Si / 285 nm SiO_2 via (a) optical microscopy, (b) AFM, and (c)–(d) SIE mapping of the top HfO_x layer and buried HfS_2, indicating homogeneous oxide regions up to 6.5 nm. We observe a higher density of signal loss (represented as white patches within the flake boundary) and thickness variance in the oxide layer of partially converted HfS_2/HfO_x, suggesting increased surface roughness compared to fully oxidised regions. (e) SIE thickness profiles showing almost perfect overlap with AFM result. Spikes in layer thickness along the flake edges are disregarded as common measurement artefacts. The oxide layer is grown via thermal oxidation in ambient conditions at 200 °C for 60 min.

data to a $HfO_x/HfS_2/HfO_x$ configuration. The resulting values for the top oxide and HfS_2 layers remain unchanged, with the bottom HfO_x thickness calculated as 0 ± 1 nm. Therefore, since the oxide thickness at the HfS_2/SiO_2 interface falls within the error margin, we maintain the previous simplified model.

The HfO_x layer is also independently parameterised using a Cauchy dispersion relation [8], assuming a transparent dielectric in the 350 to 1000 nm range [57], in order to track any fluctuations in the oxide's refractive index (figure S4 in supplementary material). For the given oxidation parameters, no improvement is observed in the accuracy of the oxide thickness calculation, therefore the EP4 library dispersion is used for all further measurements.

3.3. Heterostructure mapping

In the interest of larger-scale data acquisition of the global oxidation rather than localised behaviour, we employ the SIE mapping function, which allows us to simultaneously probe 100 μm × 100 μm areas of interest with 1 μm spatial resolution (see Methods). This enables the visualisation of complementary thickness maps for every heterostructure layer.

Figure 3 showcases this mapping capability for the example of a HfS_2 sample partially oxidised via thermal annealing at 200 °C for 60 minutes, complemented by optical microscopy (figure 3(a)) and AFM (figure 3(b)). The optical micrograph shows combined interference contrast due to the choice of SiO_2 support [58–60], which can be correlated to material conversion but has no direct translation into oxide thickness. Our ellipsometry methodology allows imaging of the buried interface and separate mapping of the semiconductor layer and its oxide (figures 3(c) and (d)).

The HfS_2 map reveals unoxidised material regions, undetectable by other non-destructive characterisation techniques, while SIE mapping of the HfO_x layer surveys oxidation uniformity, showing homogeneous oxide up to 6.5 nm for the given reaction parameters. The presence of areas of missing signal and high variance, most noticeably as blank patches in the HfO_x map, suggest higher surface roughness or heterogeneity in the oxide layer of a

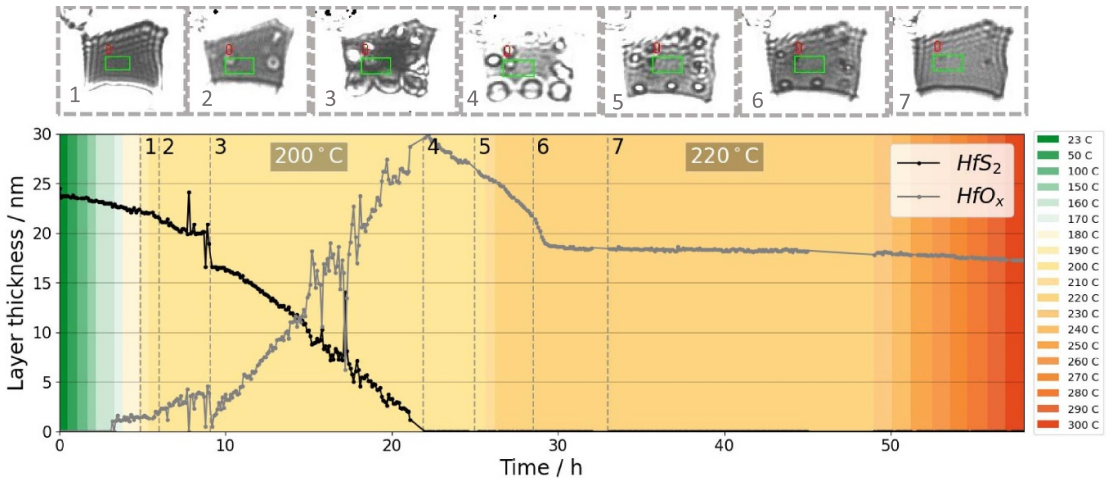

Figure 4. SIE thickness monitoring of the HfS_2 and HfO_x layers during operando oxidation of a ∼25 nm HfS_2 flake. Sample progressively oxidised by a step-wise temperature increase from room temperature to 300 °C over a 60 h time frame. Background colour corresponds to the sample temperature at the time of measurement. Upper panel shows ellipsometric contrast images captured during the measurement at oxidation points 1) 4.9 h, 190 °C; 2) 6 h, 200 °C; 3) 9.1 h, 200 °C; 4) 21.9 h, 200 °C; 5) 25 h, 200 °C; 6) 28.5 h, 220 °C; 7) 33 h, 220 °C. Signal averaged over a 10 μm × 10 μm region of interest (ROI), outlined in green and appearing distorted due to the oblique angle of view in the ellipsometer set-up. Displayed ROI is the only selection for data acquisition on this sample and thus assigned the label '0' by the EP4 software (shown in red). We observe the formation of transient blisters within the material, attributed to the accumulation and subsequent release of volatile S species during the oxidation process.

partially converted HfS_2/HfO_x heterostructure compared to fully oxidised regions. The increased oxide thickness observed along the flake edge is disregarded as a common measurement artefact, as supported by AFM. Figure 3(e) demonstrates the almost perfect overlap between the SIE thickness profiles and the AFM cross-section, confirming the optical model's accuracy and SIE's reliability as a faster, larger-scale alternative to AFM.

3.4. Operando oxidation

We observe the HfS_2 oxidation in operando for a ∼25 nm flake progressively oxidised by a step-wise temperature increase from room temperature to 300 °C over a 60 h time frame (figure 4). Each data point, corresponding to a set of (Ψ, Δ) spectra taken at 30 equidistant wavelength points along the 360 to 1000 nm range, is recorded over 6 min at 6 min intervals. The signal is averaged over an approx. 10 μm × 10 μm ROI, outlined in green on the ellipsometric enhanced contrast (ECM) images captured during the measurement (top panel of figure 4, images 1–7). The data is fitted to the previously discussed HfS_2/HfO_x model, and the thickness parameter of each layer is plotted as a function of time and temperature.

The HfO_x signal stagnates at 0 nm until 170 °C, despite the HfS_2 showing a steady decrease. This could be a consequence of inhomogeneity, reduced sensitivity to the transparent oxide compared to the stronger semiconductor signal, or an experimental limitation, as the expected ∼1–2 nm of oxide growth falls within ellipsometry measurement errors. Therefore, we assess the oxidation progression via the HfS_2 layer thickness.

It is worth noting that ellipsometry at elevated temperatures poses another challenge in terms of data analysis: the temperature dependence of the dielectric function [8] translates to the broadening and shift to lower energies of the ε peaks. Most well documented is the temperature dependence of ε_{Si} [61, 62] within the 0 to 1000 K range. Therefore, the deconvolution of the HfS_2 and HfO_x dielectric functions above room temperature can present some difficulty due to this global effect over each layer in the material stack. Given the final oxide thickness value, measured in operando by fitting to the previously discussed 'room temperature' optical model, is in good agreement with post-mortem AFM measurements, we consider the change in ε to be negligible in this temperature range for layer thickness monitoring.

The first 6 data points in figure 4 are recorded at room temperature, showing an initial decrease of ∼0.8 nm in the HfS_2 layer, comparable to the 0.68 nm monolayer thickness measured via AFM by Fu *et al* [63] and the 0.59 nm interlayer distance as calculated by Greenaway and Nitsche [51]. Exposure to ambient conditions for an additional 30 min results in no change to the HfS_2 signal, suggesting the formation of a self-limiting native oxide layer (enlargement of the data recorded during the first 5 h is shown in figure S5 of the supplementary material). The temperature is then increased to 50 °C, 100 °C, and 150 °C at 30 min intervals. We observe the thickness change occurs immediately after the temperature increase, with subsequent data points recorded at the same temperature

converging to a stable value, which suggests a self-limiting behaviour within these parameters.

The temperature is then increased in steps of 10 °C up to 200 °C, maintaining a 30 min interval with the exception of the 160 °C and 180 °C regions. At these temperatures, the signal shows greater fluctuation and has not yet stabilised to a constant value after 30 min, necessitating a doubled time frame of 1 h. After the 200 °C threshold, the oxidation accelerates and continues to full conversion of the HfS_2 into its native oxide over 10 h. Notably, this oxidation coincides with a higher level of signal instability, which can be correlated to severe roughening of the previously uniform flake and the appearance of blisters within the measured ROI (figure 4, images 2–5). Since the μm-scale surface inhomogeneity is much larger than the incident wavelength, this increase in the measurement error is expected due to partial polarisation of the reflected light [64].

Blister formation also impacts the calculated oxide thickness, which is temporarily distended to ∼30 nm before stabilising at 18.3 nm after a return to flake uniformity (figure 4, images 4–7). The HfO_x layer averages 18.3 nm for approx. 20 h of sustained exposure to 220 °C. The temperature is further increased to 300 °C, leading to a final oxide thickness of 17.3 nm, constant over 16.5 h of maintained thermal annealing. The calculated HfO_x thickness remains stable after a final temperature increase to 350 °C and 400 °C (figure S6 in supplementary material), suggesting complete oxidation.

An additional SIE measurement is performed at room temperature, indicating a 17.1 nm oxide layer and no HfS_2 present, in agreement with the final operando measurement at 400 °C. The consistency of the oxide thickness calculation across room temperature and high-temperature measurements confirms our initial assumption that temperature has a negligible effect on the ε within the 23 °C to 400 °C range.

Despite the formation of transient blisters during oxidation, the sample's surface homogeneity both before and after thermal treatment is confirmed via optical microscopy and AFM (figure S7 in supplementary material). Post-mortem AFM measurements at room temperature indicate a slight increase to 19.3 nm in sample thickness compared to the 17.1 nm measured by SIE. The 2 nm difference could be attributed to a shift in the optical properties of the HfO_x layer due to the oxidation conditions. As mentioned earlier, different oxidation parameters can impact material stoichiometry, giving rise to slight variations in the ε. This effect proved negligible for the previous samples but may be more pronounced in the case of HfO_x grown during the operando measurement, with the error compounded by the doubled oxide thickness. Beyond any uncertainty in the fitting procedure, we also consider the effect of surface roughness and signal averaging. The post-mortem AFM characterisation suggests a degree of surface inhomogeneity and thickness variation, visible as white features in the AFM image (figure S7(c) in supplementary material). While the flake appears largely uniform in the AFM cross-section (figure S7(d) in supplementary material), we note that the SIE signal is averaged over an area of 10 μm × 10 μm. Therefore, the comparison between AFM-measured and SIE-calculated thickness is less precise for the single-point measurements used during operando data acquisition, as opposed to the micron-resolved thickness maps shown in figure 3, which exhibit good overlap with the AFM profile.

The formation of blisters during the oxidation process has been reported for other TMD systems [46, 47, 65]. In the case of HfS_2, most oxidation studies mention the formation of temporary 'islands' that dissolve after prolonged oxidation time [46] or no oxide heterogeneity [33–35]. The phenomenon is studied more extensively in Se systems, specifically $HfSe_2$ [47, 65] and $TiSe_2$ [66], outlining the accumulation and retention of the less volatile Se within the interlayer spacing as an intermediate step to full oxidation. The transient nature of the blisters in our system suggests the formation of a more volatile gaseous sulphur species, most likely SO_2, as a byproduct of the oxidation reaction.

The difference in volatility for chalcogen species and their subsequent removal pathway during TMD oxidation are of great technological interest for efficient and homogeneous oxide growth. Additionally, it can impact the evaluation of material conversion through characterisation techniques such as AFM. Although the reduction in material thickness we observe after oxidation can be linked to the 1.8 : 1 volume ratio of HfS_2/HfO_2 [33], conflicting reports exist in the literature regarding this effect. Prolonged exposure to ambient air [48] and thermal annealing in air [35] have been linked to material expansion. Conversely, studies on plasma [33] and laser-assisted oxidation [34] suggest material compression, while yet another investigation into HfS_2 conversion via oxygen plasma [46] notes a thickness increase. However, the studies concurring on material expansion also report increased surface roughness, which suggests oxidation progression to a stage akin to the previously observed 'blistering' phenomenon without reaching the point of expelling volatile species trapped in the oxide.

We find that the start and end point of this 'roughening' effect, as well as the surface area and stability of the blisters, depend on multiple parameters (flake size and thickness, oxidation temperature, and ramp-up temperature profile), likely due to kinetic competition between oxidation rate and volatility of the reaction products. Figure 5 shows the example of a HfS_2 sample of similar thickness where the blisters have been preserved *ex situ* after 10 min of thermal annealing at 300 °C in ambient conditions. The presence of blisters and surface inhomogeneity is visible

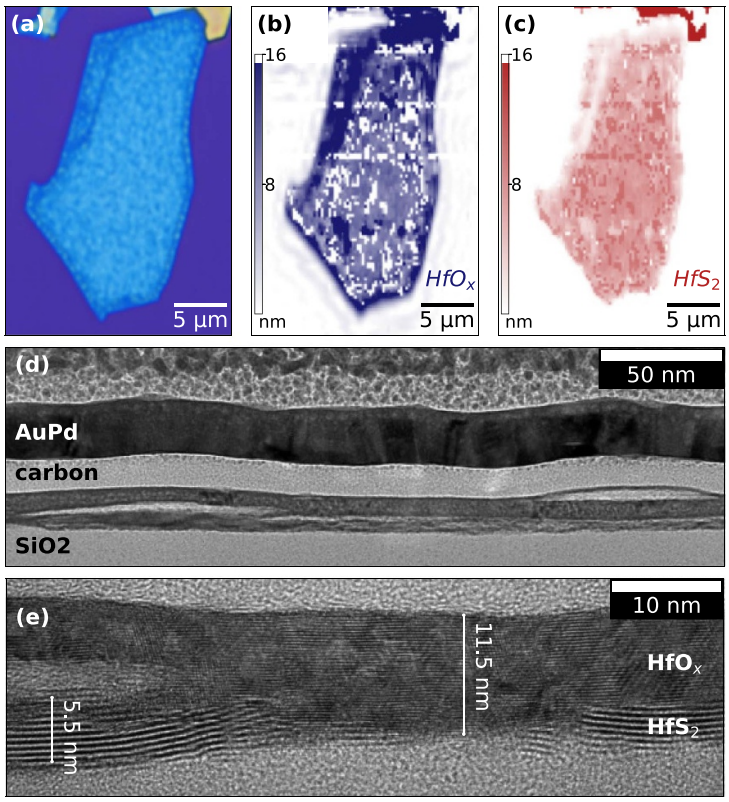

Figure 5. (a) Optical image of partially oxidised HfS_2 with visible blistering post oxidation. Sample obtained via thermal annealing in ambient conditions at 300 °C for 10 min. (b)–(c) SIE mapping of the same sample, showing an average thickness of 9.9 nm and 7.1 nm for the HfO_x and HfS_2 layers, respectively. High variance and loss of signal (represented as white regions within the flake boundary) in the HfO_x map suggest heterogeneity is mainly present within the oxide. (d)–(e) Cross-sectional HRTEM imaging of the above sample, demonstrating the presence of buried empty 'blisters' at the HfS_2/HfO_x interface and within the oxide. We observe non-uniform oxidation of the HfS_2 layers and variation in the oxide thickness between 9 and 11.5 nm. The oxide layer is largely epitaxial but presents signs of polycrystallinity.

as non-uniform contrast under optical microscopy (figure 5(a)) but also detectable via SIE mapping (figures 5(b) and (c)). Both layers exhibit signal instability and pronounced local non-uniformity, with an average oxide thickness of 9.9 nm and HfS_2 thickness of 7.1 nm. The higher noise level and signal loss in the HfO_x layer (figure 5(b)), rendered on the SIE map as white regions of zero thickness within the flake boundary, suggest the defects lie primarily within the oxide layer or at the HfS_2/HfO_x interface. We compare this to an HRTEM cross-section of the same sample (figures 5(d) and (e)), confirming the presence of stochastically distributed empty pockets across the heterostructure, both at the interface level and closer to the oxide surface. EDX elemental mapping over one such structure (figure S8 in supplementary material) indicates a complete displacement of Hf within the blister, with a remaining high density of S.

HRTEM imaging also shows polycrystallinity in the HfO_x layer, unlike the previously discussed sample and similar studies of native HfS_2 oxidation, which report an amorphous oxide [33–35]. The analysis of diffraction patterns in Fast Fourier Transform (FFT) images confirms the presence of monoclinic HfO_2 (figure S9 in supplementary material). While SIE can discern between the amorphous and crystalline polymorphs of hafnia [67, 68] via shifts in the oxide's ε, this difference is undetectable in the current context of a highly non-uniform heterostructure, analysed in a spectral range far below the oxide's absorption range (4–6 eV). Further tuning of the oxidation parameters and analysis of fully oxidised samples in a wider spectral range could paint a clearer picture of the effect of oxidation parameters on crystallinity.

4. Conclusion

We address the challenges associated with imaging and characterisation of buried interfaces in low-dimensional materials, focusing on the model system of HfS_2 oxidation. We have determined the complex dielectric function of air-sensitive HfS_2 via a versatile fitting technique on ellipsometric data obtained within an inert environment, then applied it to the modelling of partially oxidised HfS_2/HfO_x heterostructures. Through the multi-scale capabilities of SIE, we can generate high-resolution, non-destructive 3D thickness maps of the oxide and buried semiconductor layer, leading to valuable insights into oxide growth and homogeneity as a function

of reaction parameters. We showcase the operando capability of thermal HfS_2 oxidation, from pristine HfS_2 to fully converted hafnia, and the detection of self-limiting oxide growth, shedding light on its temperature and time-dependent characteristics. We observe the trapping and subsequent release of sulphur reaction products at different oxidation stages, manifested as transient blisters within the oxide layer. Further analysis of this phenomenon can yield valuable information on the kinetics of TMD oxidation and the promotion of homogeneous oxide growth.

Additional study of the material's ε at varying temperatures and layer thicknesses can help identify the essential set of probing wavelengths needed for an ellipsometric 'fingerprint'. This can expedite the evaluation of material properties, resulting in enhanced time resolution and a more comprehensive understanding of the reaction progression. Similarly, adjusting experimental parameters and utilising swifter SIE modes, such as ECM [11], may enable measurement times on the order of seconds. Given the versatility of the fitting algorithm, it can be applied to the analysis of other TMDs and their heterostructures, including materials with pronounced air sensitivity. More broadly, operando analysis of multi-layer systems is relevant to any material transformations involving the dynamic creation of a heterostructure. Our methodology enables the exploration of fundamental questions on material stability and oxidation via simultaneous analysis of the material's degradation and oxide formation.

Data availability statement

All data that support the findings of this study are included within the article (and any supplementary files).

Acknowledgments

S H acknowledges funding from EPSRC (EP/T001038/1, EP/V047515/1, EP/P005152/1). I C acknowledges funding from EPSRC (EP/N509620/1, EP/R513180/1). A A acknowledges financial support from the Saudi Arabian Ministry of Higher Education. TEM access at the University of Manchester was supported by the Henry Royce Institute for Advanced Materials, funded through EPSRC Grants EP/R00661X/1, EP/S019367/1, EP/P025021/1 and EP/P025498/1. S J H acknowledges EPSRC Grant EP/V001914/1 and the European Research Council (ERC) Under the European Union's Horizon 2020 research and innovation programme (Grant ERC-2016-STG-EvoluTEM-715502).

ORCID iDs

Irina Chircă https://orcid.org/0000-0002-0496-2763
AbdulAziz AlMutairi https://orcid.org/0000-0003-3836-6123
Barat Achinuq https://orcid.org/0000-0001-6446-8209
Sarah J Haigh https://orcid.org/0000-0001-5509-6706
Stephan Hofmann https://orcid.org/0000-0001-6375-1459

References

[1] Green M L *et al* 2017 *Appl. Phys. Rev.* **4** 011105
[2] Tabor D P *et al* 2018 *Nat. Rev. Mater.* **3** 5–20
[3] Pyzer-Knapp E O, Pitera J W, Staar P W, Takeda S, Laino T, Sanders D P, Sexton J, Smith J R and Curioni A 2022 *npj Comput. Mater.* **8** 84
[4] Stein H S and Gregoire J M 2019 *Chem. Sci.* **10** 9640–9
[5] Lemme M C, Akinwande D, Huyghebaert C and Stampfer C 2022 *Nat. Commun.* **13** 1392
[6] Stierle A and Molenbroek A M 2007 *MRS Bull.* **32** 1001–9
[7] Alberi K *et al* 2018 *J. Phys. D: Appl. Phys.* **52** 013001
[8] Fujiwara H 2007 *Spectroscopic Ellipsometry: Principles and Applications* (Wiley)
[9] Funke S, Miller B, Parzinger E, Thiesen P, Holleitner A and Wurstbauer U 2016 *J. Phys.: Condens. Matter* **28** 385301
[10] Funke S, Wurstbauer U, Miller B, Matković A, Green A, Diebold A, Röling C and Thiesen P H 2017 *Appl. Surf. Sci.* **421** 435–9
[11] Braeuninger-Weimer P, Funke S, Wang R, Thiesen P, Tasche D, Viöl W and Hofmann S 2018 *ACS Nano* **12** 8555–63
[12] Sigger F, Lambers H, Nisi K, Klein J, Saigal N, Holleitner A W and Wurstbauer U 2022 *Appl. Phys. Lett.* **121** 071102
[13] Yim C, O'Brien M, McEvoy N, Winters S, Mirza I, Lunney J G and Duesberg G S 2014 *Appl. Phys. Lett.* **104** 103114
[14] Park J W, So H S, Kim S, Choi S H, Lee H, Lee J, Lee C and Kim Y 2014 *J. Appl. Phys.* **116** 183509
[15] Yu Y *et al* 2015 *Sci. Rep.* **5** 16996
[16] Eichfeld S M, Eichfeld C M, Lin Y C, Hossain L and Robinson J A 2014 *APL Mater.* **2** 092508
[17] Maracas G N, Edwards J L, Gerber D S and Droopad R 1993 *Appl. Surf. Sci.* **63** 1–8
[18] Kim W J, Ko E K, Kim S Y, Kim B and Noh T W 2019 *Curr. Appl. Phys.* **19** 400–5
[19] Hilse M, Wang X, Killea P, Peiris F and Engel-Herbert R 2021 *J. Cryst. Growth* **566** 126177
[20] Fujiwara H, Kondo M and Matsuda A 2001 *Phys. Rev.* B **63** 115306
[21] Crovetto A, Whelan P R, Wang R, Galbiati M, Hofmann S and Camilli L 2018 *ACS Appl. Mater. Interfaces* **10** 25804–10
[22] McMarr P J, Vedam K and Narayan J 1986 *J. Appl. Phys.* **59** 694–701
[23] Vanhellemont J, Roussel P and Maes H 1991 *Nucl. Instrum. Methods Phys. Res.* B **55** 183–7
[24] McMarr P J, Mrstik B J, Barger M S, Bowden G and Blanco J R 1990 *J. Appl. Phys.* **67** 7211–22
[25] Johs B, Herzinger C, Dinan J, Cornfeld A and Benson J 1998 *Thin Solid Films* **313** 137–42
[26] Levenberg K 1944 *Q. Appl. Math.* **2** 164–8
[27] Marquardt D W 1963 *SIAM J. Appl. Math.* **11** 431–41
[28] Doherty J E and Hunt R J 2010 *Approaches to Highly Parameterized Inversion: A Guide to Using Pest for Groundwater-Model Calibration (U.S. Geological Survey Scientific Investigations Report)* vol 2010-5169 (US Department of the Interior)
[29] Kuzmenko A B 2005 *Rev. Sci. Instrum.* **76** 083108
[30] Chhowalla M, Shin H S, Eda G, Li L J, Loh K P and Zhang H 2013 *Nat. Chem.* **5** 263–75
[31] Kanazawa T, Amemiya T, Ishikawa A, Upadhyaya V, Tsuruta K, Tanaka T and Miyamoto Y 2016 *Sci. Rep.* **6** 22277

[32] Mleczko M J, Zhang C, Lee H R, Kuo H H, Magyari-Köpe B, Moore R G, Shen Z X, Fisher I R, Nishi Y and Pop E 2017 *Sci. Adv.* **3** e1700481
[33] Lai S, Byeon S, Jang S K, Lee J, Lee B H, Park J H, Kim Y H and Lee S 2018 *Nanoscale* **10** 18758–66
[34] Peimyoo N *et al* 2019 *Sci. Adv.* **5** eaau0906
[35] Wang Y Y, Huang S M, Yu K, Jiang J, Liang Y, Zhong B, Zhang H, Kan G F, Quan S F and Yu J 2020 *J. Appl. Phys.* **127** 214303
[36] Illarionov Y Y *et al* 2020 *Nat. Commun.* **11** 3385
[37] Kingon A I, Maria J P and Streiffer S 2000 *Nature* **406** 1032–8
[38] Pasquarello A, Hybertsen M S and Car R 1998 *Nature* **396** 58–60
[39] Robertson J 2005 *Rep. Prog. Phys.* **69** 327
[40] Chamlagain B, Cui Q, Paudel S, Cheng M M C, Chen P Y and Zhou Z 2017 *2D Mater.* **4** 031002
[41] Liu L, Li Y, Huang X, Chen J, Yang Z, Xue K H, Xu M, Chen H, Zhou P and Miao X 2021 *Adv. Sci.* **8** 2005038
[42] Zhang Y, Yu J, Zhu R, Wang M, Tan C, Tu T, Zhou X, Zhang C, Yu M and Gao X *et al* 2022 *Nat. Electron.* **5** 643–9
[43] Chen J, Liu Z, Dong X, Gao Z, Lin Y, He Y, Duan Y, Cheng T, Zhou Z and Fu H *et al* 2023 *Nat. Commun.* **14** 4406
[44] Li Q, Zhou Q, Shi L, Chen Q and Wang J 2019 *J. Mater. Chem.* A **7** 4291–312
[45] Deal B E and Grove A S 1965 *J. Appl. Phys.* **36** 3770–8
[46] Jin T, Zheng Y, Gao J, Wang Y, Li E, Chen H, Pan X, Lin M and Chen W 2021 *ACS Appl. Mater. Interfaces* **13** 10639–49
[47] Mirabelli G *et al* 2016 *J. Appl. Phys.* **120** 125102
[48] Chae S H *et al* 2016 *ACS Nano* **10** 1309–16
[49] Newville M, Stensitzki T, Allen D B and Ingargiola A 2015 Lmfit: Non-linear least-square minimization and curve-fitting for python (https://doi.org/10.5281/zenodo.11813)
[50] Jellison J G and Modine F 1996 *Appl. Phys. Lett.* **69** 2137–2137
[51] Greenaway D and Nitsche R 1965 *J. Phys. Chem. Solids* **26** 1445–58
[52] Roubi L and Carlone C 1988 *Phys. Rev.* B **37** 6808
[53] Li Y, Chernikov A, Zhang X, Rigosi A, Hill H M, Van Der Zande A M, Chenet D A, Shih E M, Hone J and Heinz T F 2014 *Phys. Rev.* B **90** 205422
[54] Wakagi M, Fujiwara H and Collins R 1998 *Thin Solid Films* **313** 464–8
[55] Sopra database (available at: www.sspectra.com/sopra.html)
[56] El-Shazly T S, Khedr G E and Abd El Rehim S S 2022 *Appl. Phys.* A **128** 489
[57] Waldorf A J, Dobrowolski J A, Sullivan B T and Plante L M 1993 *Appl. Opt.* **32** 5583–93
[58] Blake P, Hill E, Castro Neto A, Novoselov K, Jiang D, Yang R, Booth T and Geim A 2007 *Appl. Phys. Lett.* **91** 063124
[59] Li H, Wu J, Huang X, Lu G, Yang J, Lu X, Xiong Q and Zhang H 2013 *ACS Nano* **7** 10344–53
[60] Puebla S, Li H, Zhang H and Castellanos-Gomez A 2022 *Adv. Photon.* **3** 2100221
[61] Jellison J G and Modine F 1994 *J. Appl. Phys.* **76** 3758–61
[62] Lautenschlager P, Garriga M, Vina L and Cardona M 1987 *Phys. Rev.* B **36** 4821
[63] Fu L *et al* 2017 *Adv. Mater.* **29** 1700439
[64] Lee J, Rovira P I, An I and Collins R 1998 *Rev. Sci. Instrum.* **69** 1800–10
[65] Shen Y, Yang J, Yuan Y, Jing Y, Yi Y, Liu X and Sun J 2023 *Phys. Status Solidi* **17** 2300067
[66] Sun L *et al* 2017 *Angew. Chem., Int. Ed.* **56** 8981–5
[67] Pavoni E, Mohebbi E, Mencarelli D, Stipa P, Laudadio E and Pierantoni L 2022 *Nanomaterials* **12** 4324
[68] Tan T, Liu Z, Lu H, Liu W and Tian H 2010 *Opt. Mater.* **32** 432–5